

Real-time analysis of T cell receptors in naive cells in vitro and in vivo reveals flexibility in synapse and signaling dynamics

Rachel S. Friedman, Peter Beemiller, Caitlin M. Sorensen, Jordan Jacobelli, and Matthew F. Krummel

Department of Pathology, University of California, San Francisco, San Francisco, CA 94143

The real-time dynamics of the T cell receptor (TCR) reflect antigen detection and T cell signaling, providing valuable insight into the evolving events of the immune response. Despite considerable advances in studying TCR dynamics in simplified systems in vitro, live imaging of subcellular signaling complexes expressed at physiological densities in intact tissues has been challenging. In this study, we generated a transgenic mouse with a TCR fused to green fluorescent protein to provide insight into the early signaling events of the immune response. To enable imaging of TCR dynamics in naive T cells in the lymph node, we enhanced signal detection of the fluorescent TCR fusion protein and used volumetric masking with a second fluorophore to mark the T cells expressing the fluorescent TCR. These in vivo analyses and parallel experiments in vitro show minimal and transient incorporation of TCRs into a stable central supramolecular activating cluster (cSMAC) structure but strong evidence for rapid, antigen-dependent TCR internalization that was not contingent on T cell motility arrest or cSMAC formation. Short-lived antigen-independent TCR clustering was also occasionally observed. These in vivo observations demonstrate that varied TCR trafficking and cell arrest dynamics occur during early T cell activation.

CORRESPONDENCE

Matthew F. Krummel:
matthew.krummel@ucsf.edu

Abbreviations used: cSMAC, central supramolecular activating cluster; pMHC, cognate peptide-MHC; PMT, photo-multiplier tube; TIRF, total internal reflection fluorescence.

Real-time in vivo imaging has enhanced our understanding of cellular motility and cell-cell interactions during processes such as T cell activation. Two-photon imaging studies of T cell activation in the LN show multiple stages of T cell-DC interactions after antigen recognition (Mempel et al., 2004; Miller et al., 2004), which can vary from the dynamics observed in in vitro settings. In vitro imaging has provided enormous insight into the molecular dynamics of the TCR during T cell activation (Cemerski and Shaw, 2006; Dustin et al., 2006). However, T cell activation behaviors appear to vary depending on the model system used (Grakoui et al., 1999; Gunzer et al., 2000; Krummel et al., 2000; Brossard et al., 2005), raising questions about the relationship between TCR dynamics and cellular motility.

The formation of a highly stable immunological synapse is the predominant paradigm for T cell signaling, characterized by immediate firm adhesion to the opposing membrane, followed within the first 2 min by calcium signaling (Wülfing et al., 1997), tyrosine phosphorylation

(Lee et al., 2002), and clustering of the TCR (Grakoui et al., 1999; Krummel et al., 2000; Wülfing et al., 2002). Coalescence of initial TCR clusters gives rise to a mature immunological synapse with a characteristic central supramolecular activating cluster (cSMAC) of TCRs surrounded by concentric rings of adhesion and auxiliary molecules such as LFA-1 (Monks et al., 1998; Grakoui et al., 1999). A downstream effect of TCR signaling is TCR internalization and degradation. TCR internalization increases with antigen dose and potency (Hemmer et al., 1998; Liu et al., 2000), with ligands that induce stronger functional responses causing more TCR downmodulation as the result of more complete phosphorylation of TCR complex ITAMs (immunoreceptor tyrosine-based activation motif; Itoh et al., 1999). Ultimately, antigen-dependent TCR internalization

© 2010 Friedman et al. This article is distributed under the terms of an Attribution-Noncommercial-Share Alike-No Mirror Sites license for the first six months after the publication date (see <http://www.rupress.org/terms>). After six months it is available under a Creative Commons License (Attribution-Noncommercial-Share Alike 3.0 Unported license, as described at <http://creativecommons.org/licenses/by-nc-sa/3.0/>).

leads to lysosome- and proteasome-dependent TCR degradation (Valitutti et al., 1997; Liu et al., 2000). The cSMAC has been implicated as a site of signal termination that is enriched for LBPA (lysobisphosphatidic acid), a lipid associated with sorting of membrane proteins for degradation through multivesicular bodies (Varma et al., 2006).

Contrary to this understanding, naive T cells interacting with antigen-bearing DCs *in vitro* predominantly form multifocal TCR polarizations (Brossard et al., 2005) rather than the classical cSMAC conformation. Also, naive T cell activation occurs in the apparent absence of sustained arrest in an *in vitro* system using DCs embedded in a collagen matrix (Gunzer et al., 2000), suggesting that prolonged synapse assembly is not necessary for T cell activation.

Similarly, many but not all *in vivo* observations of T cell activation in the LN have shown short-lived encounters with antigen-bearing APCs as a prelude to stable interactions (Miller et al., 2002; Bousso and Robey, 2003; Mempel et al., 2004). The up-regulation of activation markers on T cells that only had transient interactions with DCs suggests that TCR signaling occurs during these transient interactions (Mempel et al., 2004); however, it has been shown that prolonged interactions may be necessary for full effector function acquisition (Hurez et al., 2003; Scholer et al., 2008) and memory formation (Scholer et al., 2008). It has recently been proposed that motile interactions with antigen-presenting surfaces should be separately described as kinapses (Dustin, 2007), although it remains to be determined *in vivo* how the signaling and trafficking dynamics of the TCR relate to motility.

Antigen-independent T cell–DC synapses leading to polarization of the TCR have been observed *in vitro* and can lead to increases in local phosphotyrosine levels, low level calcium fluxes, and weak proliferation (Revy et al., 2001; Stefanová et al., 2002). These antigen-independent interactions promote the recognition of foreign antigen by maintaining a basal level of T cell activation (Stefanová et al., 2002).

Molecular-level imaging of receptor fusions *in vivo* has been limited to mostly transparent organisms such as zebrafish (Jontes et al., 2004). The only dynamic molecular imaging in the LN to date has shown that LAT (linker of activated T cells) localizes to the contact interface during stable interactions of activated T cells with antigen-bearing B cells but not during motile interactions of activated T cells with DCs (Azar et al., 2010). Static imaging of CD43–GFP fusion proteins also demonstrated T cell–DC interactions that exclude CD43 from the contact interface (Stoll et al., 2002), which is consistent with this molecule's position in synapses formed *in vitro*. Imaging TCR localization under fixed conditions during antigen recognition *in vivo* showed TCR polarization toward the DC (Reichert et al., 2001; McGavern et al., 2002; Barcia et al., 2006; Khanna et al., 2007), although the dynamics of this phenotype are unknown. *In vivo* imaging of fluorescent fusion proteins expressed at physiological levels allows for tracking of surface and internal pools of receptors but has been impeded by low fluorescence signal. Lymphoid tissues provide additional challenges because they are highly autofluorescent

and they refract and absorb the low specific signal of fluorescent fusions. Thus, it remains unclear whether TCR clustering associated with mature immunological synapse formation is involved in primary activation of naive T cells and how the lymphoid environment affects T cell signal initiation.

Our goals were to provide insight into the early events of naive T cell signaling during antigen recognition *in situ* and to test whether cSMAC formation was an essential signaling event. To do so, we generated a transgenic mouse expressing a TCR–GFP fusion and imaged the TCR dynamics in naive cells in the LN in response to their initial encounter with antigen. Our data demonstrate that in the absence of cognate antigen, naive T cells infrequently and transiently clustered but did not internalize their TCR. However, after their initial interaction with antigen-bearing DCs, TCR clustering was rapid, brief, and quickly led to internalization. Additionally, TCR internalization did not depend upon stable or prolonged cSMAC-like TCR clustering. In the intact LN, although TCR clustering and internalization frequently followed T cell arrest, neither were contingent upon arrest. Our results indicate that continued T cell motility does not imply an absence of TCR triggering and provides evidence for a flexible relationship between motility and synapse formation. Furthermore, this highlights that cSMAC formation is not diagnostic of the presence of antigen or of successful signaling *in vivo*.

RESULTS

Expression and functionality of the OT-I–GFP TCR

Our goal was to image TCR dynamics in naive T cells in the LN in response to their initial encounter with antigen. To do this, we generated a TCR transgenic mouse expressing the α/β heterodimer of the OT-I TCR (Hogquist et al., 1994) with an unstructured linker and a single enhanced GFP fused to the C terminus of the α chain. The tagged α chain was expressed under the CD4 enhancer and promoter without the silencer (Sawada et al., 1994), and the OT-I– β chain was expressed under its endogenous promoter (Hogquist et al., 1994). We chose to GFP tag the OT-I TCR, which is specific for the chicken egg OVA–derived SIINFEKL peptide (SL8) in the context of the MHC class I molecule H2–k^b because it is well characterized and a variety of tools exist to facilitate its use.

Expression of the OT-I–GFP TCR was limited to the CD8 T cell lineage because of the use of T cell–specific promoters and MHC class I restriction (Fig. 1 a). Allelic exclusion limited the expression of other TCRs; however, to eliminate remaining endogenous TCR rearrangement and expression, we crossed the OT-I–GFP mice onto the Rag2^{-/-} background. Surface expression of the OT-I–GFP TCR was confirmed by surface staining for the α and β chains of the OT-I TCR using V α 2- and V β 5-specific antibodies. In OT-I–GFP Rag2^{-/-} mice, GFP expression was linearly related to surface expression of both the α and β TCR chains (Fig. 1 b).

To confirm that the GFP tag did not disrupt TCR localization or signaling, we directly compared WT OT-I versus OT-I–GFP T cells using a variety of functional and

imaging-based assays. The dynamics of TCR microcluster and cSMAC formation were assessed by imaging of the TCR on supported planar lipid bilayers presenting cognate peptide–MHC (pMHC) and ICAM-1. WT OT-I T cells and OT-I-GFP

T cells showed virtually identical kinetics of TCR microcluster formation and centralization using fluorescent surface labeling of the TCR with the H57 anti-TCR- β antibody (Fig. 1 c and Video 1). Additionally, H57 staining and the

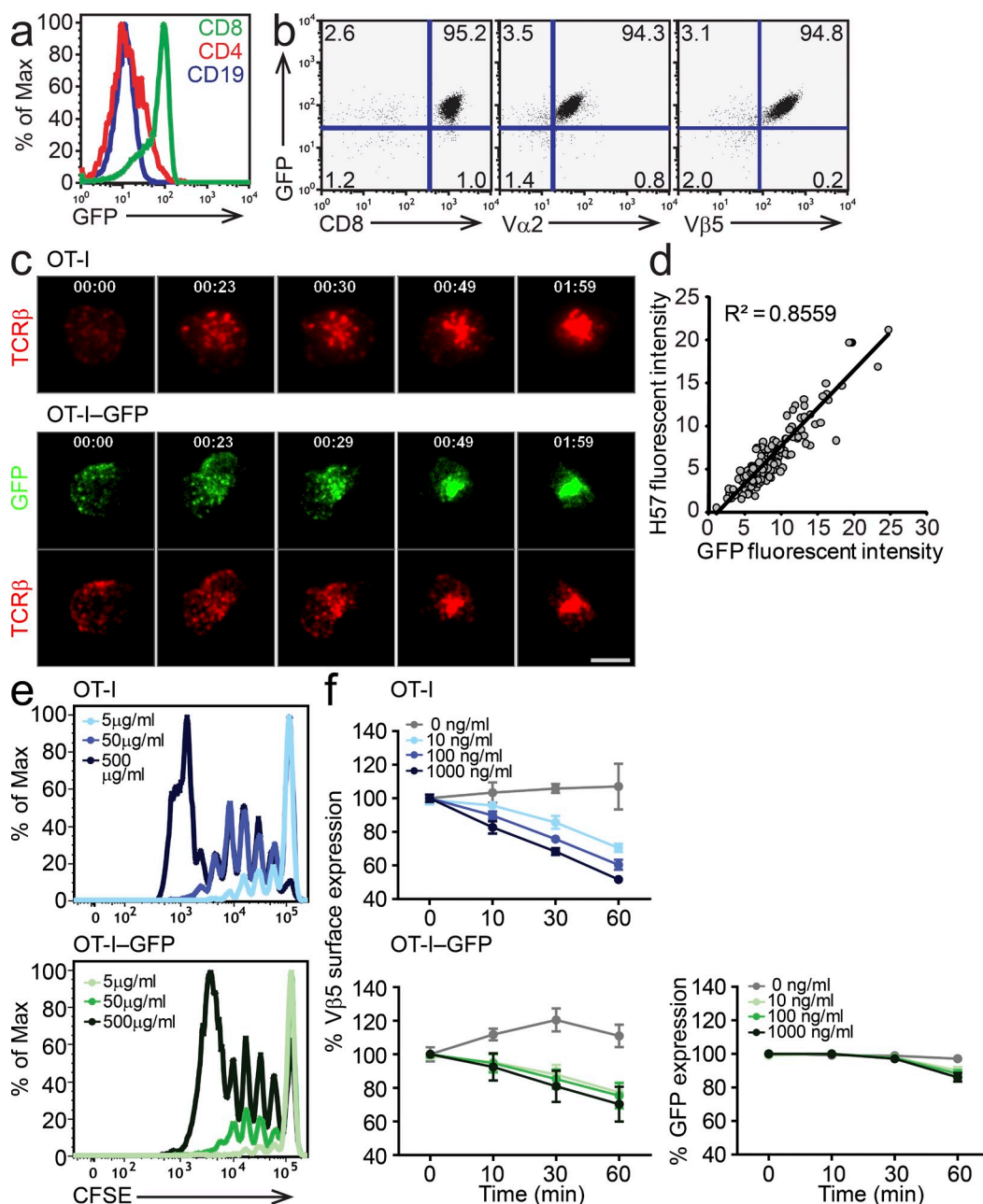


Figure 1. OT-I-GFP TCR is expressed on the cell surface and is functional. (a) Flow cytometric analysis of GFP fluorescence in OT-I-GFP LN cell subsets expressing the indicated surface markers. (b) Flow cytometric analysis of GFP fluorescence and TCR surface expression in OT-I-GFP Rag2^{-/-} LN cells. Anti-V α 2 and anti-V β 5 stain the OT-I-GFP α and β chains, respectively. Percentages are shown in each quadrant. (c and d) Naive WT OT-I or OT-I-GFP T cells were surface labeled with anti-TCR- β antibody, placed on a lipid bilayer presenting pMHC and ICAM-1, and imaged by TIRF microscopy. (c) Dynamics of microcluster and cSMAC formation. See Video 1 for full time lapse. Data are representative of two experiments. Bar, 10 μ m. (d) Quantification of fluorescent intensity of surface labeling of TCR- β (H57) and GFP of OT-I-GFP TCR microclusters. (e) Proliferation of WT OT-I CD45.1 T cells versus OT-I-GFP Rag2^{-/-} T cells. CFSE dilution of cotransferred T cells 66 h after SL8 peptide + CFA immunization. (a, b, and e) Data are representative of at least three experiments. (f) TCR down-regulation in naive T cells after stimulation with antigen-pulsed DCs. Error bars represent SEM. (d and f) Data were pooled from two experiments.

OT-I-GFP fluorescence in individual microclusters were linearly related (Fig. 1 d), and no pools of unlabeled GFP were observed, suggesting that the clusters originated on the cell surface. The functionality of the OT-I-GFP TCR was further confirmed by *in vivo* proliferation of naive WT OT-I versus OT-I-GFP T cells in response to SL8 peptide and CFA. When evaluated in competition with each other, proliferation of both WT OT-I and OT-I-GFP T cells in the draining LNs increased with antigen dose. Although OT-I-GFP T cells showed slightly reduced proliferation, it should be noted that CFSE dilution could not be tracked beyond the fourth division in the OT-I-GFP T cells because of the green fluorescence contributed by the GFP (Fig. 1 e). TCR internalization in response to antigen presented on bone marrow-derived DCs (Fig. 1 f) and T cell-DC conjugate formation (Fig. S1 a) occurred at the same rate over a range of antigen doses. Additionally, activated OT-I-GFP T cells showed similar levels of specific cytotoxicity as WT OT-I T cells (Fig. S1 b). The strikingly similar kinetics of various functional indicators of T cell signaling over a range of antigen doses exhibited by the OT-I-GFP T cells versus WT OT-I T cells indicated that the TCR behavior was unchanged and that cells were able to signal through the GFP-tagged TCR.

cSMAC-independent TCR internalization after antigen recognition on DCs

We initially sought to define TCR localization in naive T cells after antigen recognition on DCs through *in vitro* live imaging. For these experiments, OT-I-GFP T cells were mixed with antigen-pulsed LPS-matured DCs and imaged by epifluorescence microscopy. The dynamics of T cell-DC contact, synapse formation (tight apposition of T cell-DC membranes), cSMAC formation (clustering of the TCR at the T cell-DC interface), and TCR internalization were quantified in naive and previously activated OT-I-GFP T cells. These data revealed that cSMAC formation and TCR internalization were highly antigen dependent in both naive and activated T cells with little change in rate or frequency over a 2-log range of antigen dose (Fig. 2, a, b, and e). The frequency of cSMAC formation in naive cells was low (Fig. 2, a and e). Instead, TCR clusters bypassed cSMAC formation and rapidly proceeded to TCR internalization (Fig. 2 d and Video 3). When cSMACs were observed, they persisted for similar periods in naive and activated T cells (mean <10 min; Fig. 2 b).

TCR internalization occurred rapidly in both naive (Fig. 2, a, c, and d; Videos 2, 3, and 9; and see Fig. 8 d) and activated T cells (Fig. 2 a), with TCR internalization occurring significantly more frequently than cSMAC formation in naive T cells (Fig. 2 e). Analysis of cSMAC-independent TCR internalization events revealed that this was the predominant mode of internalization for naive T cells (Fig. 2 f). This internalization mode occurred more frequently in naive than activated T cells, particularly at higher antigen doses (Fig. 2 f). In both cSMAC-dependent and -independent internalization modes, internalization occurred at or near the interface with

the DC (Fig. 2, c and d; Videos 2, 3, and 9; and see Fig. 8 d), with internalized TCRs likely originating from microclusters in the cSMAC-independent mode (Fig. 2 d and see Fig. 8 d). Notably, naive T cells on lipid bilayers always rapidly formed cSMACs after antigen recognition (Fig. 1 c and not depicted), suggesting that the predominance of cSMAC-independent TCR internalization seen during T cell-DC interactions is likely to be dependent at least in part on the nature of the APC or activating surface under study. In sum, the TCR-GFP fusion provides evidence for a flexible ongoing internalization process during interactions with antigen-bearing DCs and suggests that visualization of internalized TCR represents a more robust readout of TCR engagement than cSMAC assembly.

Optimizing two-photon detection of low fluorescent signal

To assess the levels of the OT-I-GFP TCR relative to endogenously rearranged V α 2⁺ or V β 5⁺ TCRs, we transferred OT-I-GFP Rag2^{-/-} T cells into WT hosts and assessed the expression of V α 2 and V β 5 on the endogenous and the transferred T cells in the LN. Surface expression of the OT-I-GFP TCR was ~30% of that expressed by WT T cells (Fig. 3 a). Previous quantifications showed that naive T cells express 20–40,000 TCRs on the cell surface (Labrecque et al., 2001). Therefore, we estimate that OT-I-GFP Rag2^{-/-} T cells express in the range of 6–12,000 OT-I-GFP molecules on their cell surface.

Under optimal two-photon imaging conditions using cells labeled with vital dyes such as CFSE, fluorescence levels are ~3 logs above background fluorescence. However, when imaging molecular fusion proteins, the fluorescence is limited by the physiological expression levels of the molecule of interest, as well as by the extinction coefficient and quantum efficiency of the fluorophore used. In the case of OT-I-GFP T cells, the fluorescence levels were only ~1 log above the background fluorescence levels of unlabeled lymphocytes (Fig. 1 a). Therefore, to successfully image the low level fluorescence of OT-I-GFP T cells *in vivo*, it was necessary to optimize the detection of the limited GFP fluorescence. To do this, we used a custom-designed two-photon instrument with a simplified, efficient path to the photomultiplier tube (PMT) detector (Bullen et al., 2009) and a highly sensitive GaAs PMT (H7422P) on the green channel to improve detection of the OT-I-GFP signal.

To estimate the sensitivity and limitations of our system for molecular imaging, we transferred OT-I-GFP Rag2^{-/-} cells into WT hosts and imaged them by two-photon microscopy in superficial areas of the LN. We colabeled the T cells with the red dye CMTMR to provide a second mechanism for identifying the transferred cells. The GFP images were corrected for bleed-through from the CMTMR label through linear unmixing (see details in next section and Fig. 4). We then identified pixels on the cell surface of OT-I-GFP Rag2^{-/-} cells using a localized active contour segmentation algorithm (Lankton and Tannenbaum, 2008) on the GFP images (Fig. 3 b). This algorithm effectively identified a region that covered the cell surface of the OT-I-GFP cell of interest

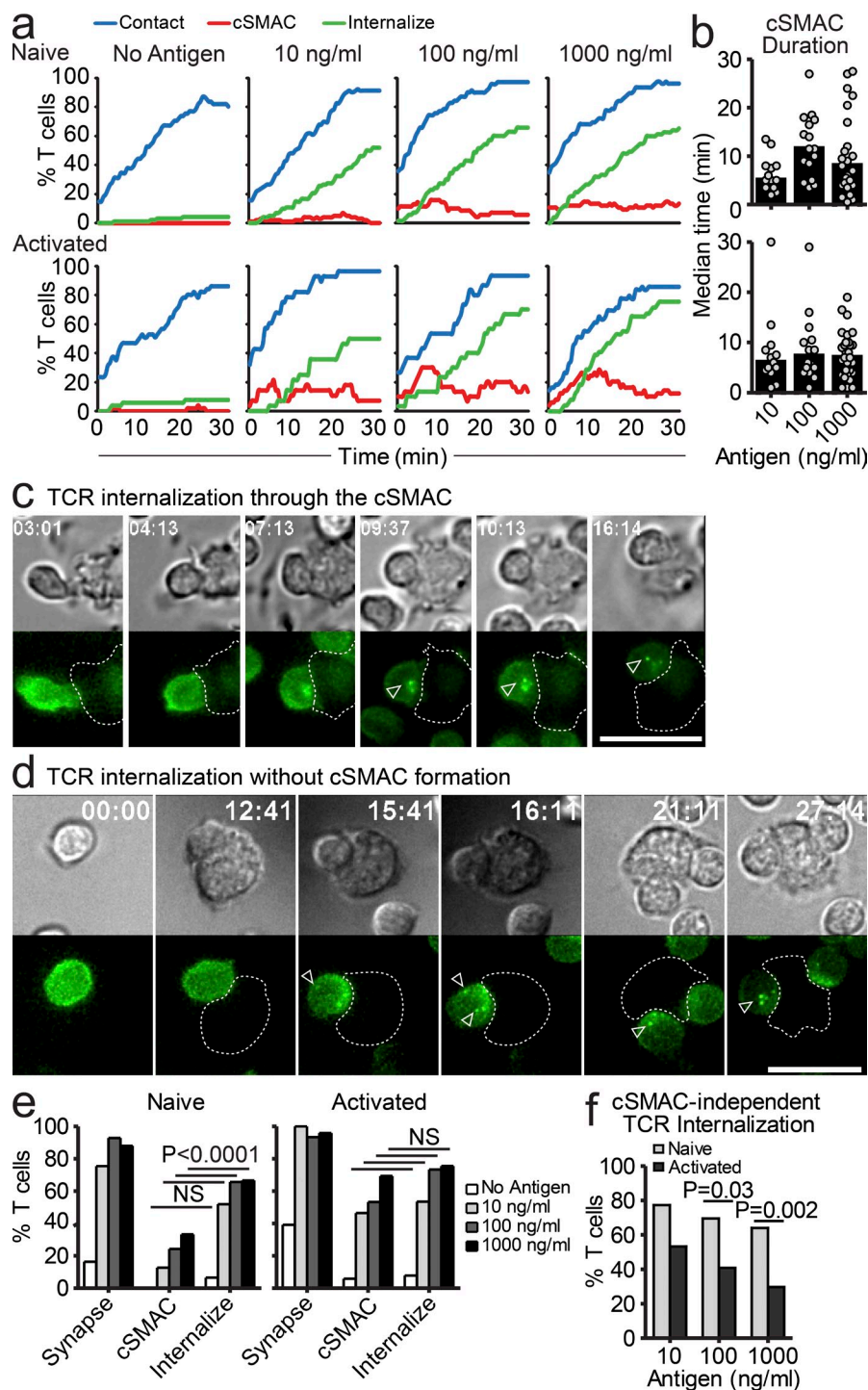


Figure 2. TCR internalization does not require cSMAC formation. Naive or activated OT-I-GFP T cells were incubated with DCs pulsed with SL8 peptide and imaged by epifluorescence microscopy. Data were pooled from two experiments. For naive T cells, $n > 60$ cells per condition. For activated T cells, $n > 30$ cells per condition. P-values were determined using Fisher's exact test. (a) TCR dynamics. The percentages of T cells in contact with DCs (contact), with a cSMAC, or with internalized TCR are indicated. Only T cells that contacted a DC during the time lapse are included. (b) Duration of cSMAC persistence. Only T cells that formed a cSMAC are included. Each dot represents one cell, and the bars represent the median. (c and d) Naive T cell-DC interactions. Contrast (top) and maximum intensity z projection of OT-I-GFP fluorescence (bottom) imaged by epifluorescence microscopy are shown. The dotted line indicates the DC border, and the arrowheads indicate internalized TCR vesicles. Bars, 10 μ m. (c) The T cell contacts the antigen-bearing DC (1,000 ng/ml SL8), stops crawling and adopts a rounded morphology, forms a cSMAC, and then internalizes vesicles of TCR through the cSMAC. See [Video 2](#) for full time lapse. (d) The T cell contacts the antigen-bearing DC (10 ng/ml SL8), forms microclusters at the T cell-DC interface, and then rapidly internalizes the TCR without forming a cSMAC. See [Video 3](#) for full time lapse. (e) Frequency of TCR behaviors. (f) Frequency of cSMAC-independent TCR internalization. Only cells that internalized their TCR are included; those that did not form a cSMAC are designated cSMAC independent.

and was sufficiently sensitive to characterize the surface distribution of the 6–12,000 GFP molecules.

Isolating dim OT-I-GFP fluorescence from tissue autofluorescence

Although we gained sufficient sensitivity to visualize the OT-I-GFP TCR in regions with low autofluorescence (Fig. 3 b), it was evident that specific signal discrimination in regions of high endogenous autofluorescence represented a significant additional challenge

(Fig. 3, b and c). We quantified the fluorescence of OT-I-GFP molecules in the identified surface regions (Fig. 3 d), which showed $14,000 \pm 7,800$ (mean \pm SD) fluorescence intensity counts from the total T cell surface or a mean of 18.5 counts/voxel. Using this quantification together with the estimate of TCR surface expression, we approximate that our instrumentation was able to register about one intensity unit (count) per OT-I-GFP molecule

(Fig. 4 a). To assess the relative intensity of OT-I-GFP fluorescence and tissue autofluorescence, we labeled OT-I-GFP T cells with CMTMR (to allow for their positive identification) and transferred them into WT hosts. In areas of the LN containing bright autofluorescence, the green fluorescence of the OT-I-GFP T cells was indistinguishable from the autofluorescence (Fig. 4 a). In highly autofluorescent areas of the LN, the frequency of bright pixels (>25 counts) contributed

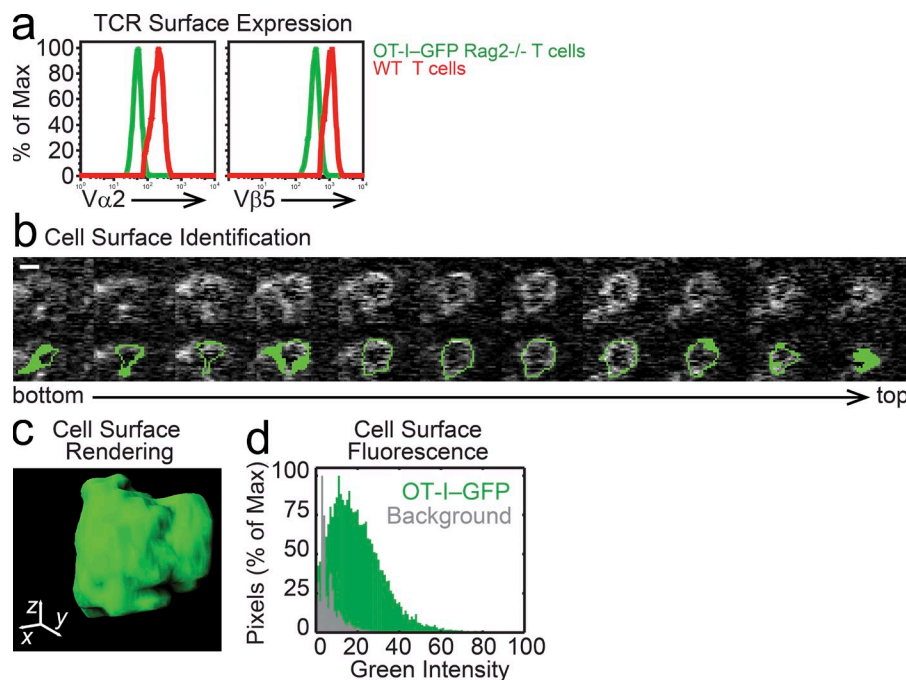


Figure 3. Quantification of OT-I-GFP T cell surface TCR fluorescence in vivo.

(a) TCR expression on the surface of OT-I-GFP Rag2^{-/-} T cells versus WT T cells with endogenously rearranged V α 2⁺ or V β 5⁺ TCRs. Data are representative of more than three experiments. (b–d) A localized active contour algorithm was used to identify the cell edges of OT-I-GFP Rag2^{-/-} cells in LNs from two-photon images. GFP images were masked in the cell surface regions. $n = 27$ cells from three experiments. (b) Representative cell surface identified by the local contour segmentation. Z-series images of an OT-I-GFP Rag2^{-/-} cell (top row) with a mask marking the surface-exposed pixels of the cell (green in bottom row). The interplane distance is 1 μ m. Bar, 4 μ m. (c) Surface volume rendering of an OT-I-GFP cell segmented using the active contour algorithm. (d) Quantification of green fluorescence of OT-I-GFP cells masked on the cell surface voxels.

by autofluorescence was >20 times greater than that contributed by OT-I-GFP T cells (Fig. 4, a and b). This autofluorescence was contributed in part by macrophages and DCs (Fig. 4 c).

We devised a data processing strategy using fluorescent colabeling and volumetric image masking to separate OT-I-GFP cells from the autofluorescence (Fig. 4 f and Video 4). The CMTMR colabeling allowed us to identify the full T cell volume. To determine the amount of bleed-through fluorescence in the green channel contributed by CMTMR fluorescence, fluorescence levels of CMTMR-labeled WT OT-I cells in LNs were measured in the red and green channels (Fig. 4 d). Data were acquired using standardized settings for all parameters. With a 525/50-nm filter on the green channel, the majority of the green signal was contributed by CMTMR fluorescence bleed-through into the green channel (Fig. 4 d). The use of a more restrictive 510/20-nm filter reduced the bleed-through and autofluorescence while still allowing for GFP detection (Fig. 4, d and e).

Using the red and green fluorescence values of CMTMR-labeled WT OT-I cells, we fitted linear equations to the data points (Fig. 4 d; see Materials and methods for equations) and used these equations to remove CMTMR bleed-through in the green channel (Fig. 4 f). Next, to mask out autofluorescence in the green channel, we made a volumetric binary mask using a simple threshold on CMTMR in the red channel (Fig. 4 f). Application of this threshold left only data contributed by CMTMR-labeled cells and extremely bright areas of autofluorescence (Fig. 4 f). Although both filters yielded usable data, the 510/20-nm filter was preferable because of the improved ratio of specific signal to CMTMR bleed-through. The reduced degree of linear unmixing required using the 510/20-nm filter allowed for more complete elimination of bleed-through from CMTMR (Fig. 4 e).

Using this protocol on data collected with both the 525/50- and 510/20-nm filters allowed clear visualization of the specific fluorescence, revealing the membrane distribution of OT-I-GFP while eliminating the vast majority of green autofluorescence (Fig. 4 e). Because the CMTMR labeling conditions and image acquisition settings were standardized, we were able to standardize the image processing for our data depending on the filter usage. Even using this protocol, OT-I-GFP-specific fluorescence visualization was limited to the superficial ~ 80 μ m of the LN because of attenuation of the dim fluorescent signal with tissue depth.

Antigen recognition results in reduced crawling speed, increased frequency of stopping, and increased duration of contacts with DCs

Because the OT-I-GFP fluorescence detection was at the limit of current technologies, we were unable to visualize the OT-I-GFP TCR together with fluorescently labeled DCs because the emission spectra overlapped too much to be able to resolve the dim OT-I-GFP fluorescence. Therefore, we chose two alternate approaches. First, we defined the kinetics of T cell–DC interactions using timed perfusion of peptide into the LN. We subsequently measured the TCR dynamics under the same conditions, inferring the relationships with DCs by choosing conditions that favored T cell–DC interactions. Second, we used anti-DEC205:OVA immunization (Bonifaz et al., 2004) to target antigen to DCs to ensure that TCR dynamics could be observed when antigen presentation was limited to DCs.

In the first instance, we required a system that synchronized early antigen recognition events and was highly biased toward T cell activation on DCs. To do this, we initially imaged the cellular dynamics of T cells in an explanted LN in the absence of

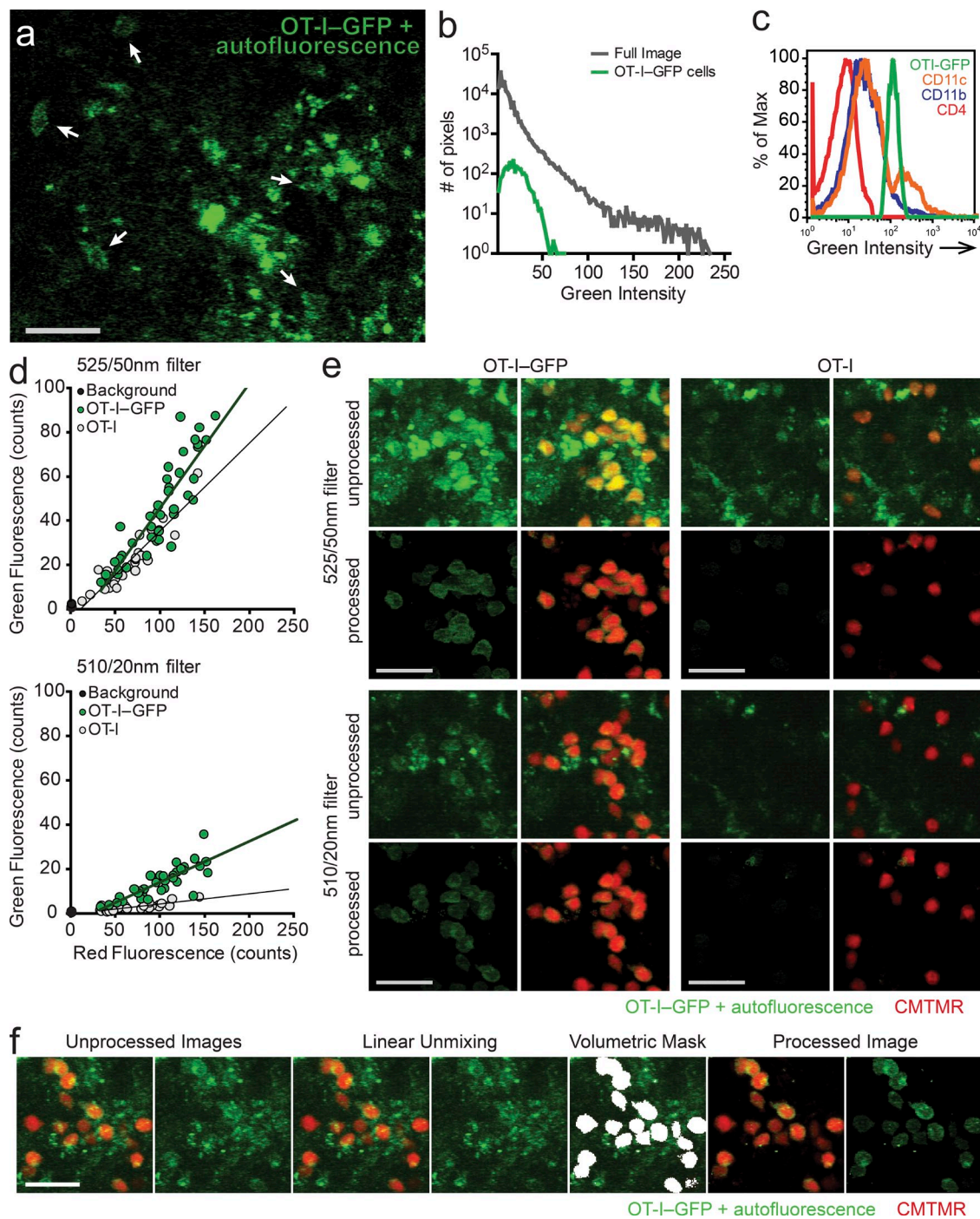


Figure 4. OT-I-GFP fluorescence can be differentiated from tissue autofluorescence. (a, b, and d–f) CMTMR (red)-labeled OT-I or OT-I-GFP Rag2^{-/-} cells (green) were transferred into WT recipients, and LNs were visualized by two-photon microscopy. Data are representative of more than three experiments. (a) Green fluorescence in a single z plane. Arrows indicate the location of OT-I-GFP Rag2^{-/-} T cells, as determined by CMTMR fluorescence (not depicted). (b) Pixel intensities in the green channel from the image represented in panel a. (c) Flow cytometric analysis of green fluorescence and autofluorescence in WT LN containing OT-I-GFP Rag2^{-/-} cells. (d) Analysis of green fluorescence contributed by CMTMR bleed-through when imaged using 525/50- versus 510/20-nm filters. Background measurements were taken in regions that did not contain tissue. Fluorescence values in the red and green channels were measured in regions that were drawn around individual OT-I or OT-I-GFP Rag2^{-/-} cells based on CMTMR. Lines represent linear equations fit to the data. See Materials and methods for the equations. (e) Representative images of maximum intensity z projections showing unprocessed and processed images. (f) Representative maximum intensity z projection at various stages of image processing. Image was acquired with the 510/20-nm filter. See [Video 4](#) for three-dimensional reconstruction of image processing. The region shown represents a tissue volume of 150 (x) × 150 (y) × 80 μm (z). Bars, 25 μm.

cognate antigen. Then, to image T cell behavior in the presence of cognate antigen, we added the OT-I agonist peptide (SL8) to the oxygenated media bathing the LN. Because the SL8 peptide is a small 8-aa peptide, we reasoned that it would be able to diffuse through the LN capsule and bind to H2-k^b on the surface of DCs within the LN. We transferred CMTMR-labeled OT-I-GFP Rag2^{-/-} T cells and actin-CFP polyclonal CD8 T cells into CD11c-YFP mice that were immunized with CFA in the footpad. The CFA induced an inflammatory milieu in the draining popliteal LN, resulting in mild increases in ICAM-1 and CD40 expression by resident DCs (Fig. S2) and likely pleiotropic effects enhancing T cell arrest (Hugues et al., 2004). 18 h after immunization and cell transfer, the popliteal LNs were explanted and imaged by two-photon microscopy. This allowed us to characterize OT-I-GFP T cell behavior and interactions with DCs before and after antigen recognition.

Because we knew that our detection of the TCR was depth restricted, we also limited our analysis of cellular dynamics to the shallow interfollicular regions of the T zone. After antigen addition to the LN, OT-I-GFP T cells reduced their displacement (Fig. 5 a) and crawling speed (Fig. 5 b), increased their duration of motility arrest (Fig. 4 c), and increased the duration of contacts with DCs (Fig. 5 d), whereas cotransferred polyclonal T cells did not (Fig. 5 and Video 5).

(Worbs et al., 2007). We also noted that areas lacking DCs (Video 5, top left quadrant) also lacked arrested OT-I-GFP T cells, suggesting that DCs were required to mediate cell slowing. The majority of arrested and slow moving OT-I-GFP T cells were directly in contact with DCs, confirming that T cells were primarily recognizing antigen on these cells in our system (Video 5).

Naive T cells in the LN exhibit occasional antigen-independent TCR clustering

Having established techniques for isolating the low specific fluorescence of the OT-I-GFP, we first analyzed TCR dynamics of naive T cells in the LN in the absence of cognate antigen (Figs. 6 a and 7). CMTMR-labeled OT-I-GFP Rag2^{-/-} cells were transferred into WT mice that were immunized with CFA in the footpad. 18 h after immunization, the draining popliteal and nondraining maxillofacial LNs were explanted and imaged by two-photon microscopy. In the absence of antigen, TCRs were mainly confined to the cell surface without consistent polarity in crawling or stopped cells; however, a small percentage of T cells clustered their TCR (Fig. 6 a; Fig. 7, a-c; and Fig. S3 a). This clustering in the absence of cognate antigen was an infrequent event (Fig. 7 a). Antigen-independent TCR clustering occurred randomly within the imaging window (Fig. 7, a and b), was transient, lasting only 2.6 ± 0.9 min (Fig. 7, b and d), and

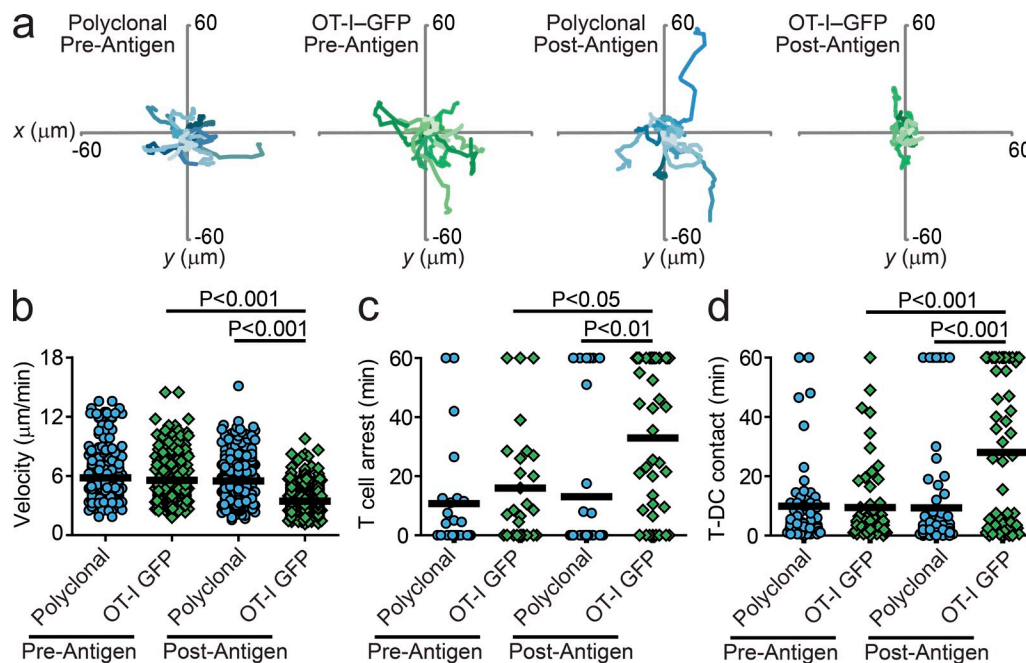


Figure 5. Motility of T cells during antigen recognition. CMTMR-labeled OT-I-GFP Rag2^{-/-} cells and CFP⁺ polyclonal CD8 T cells were cotransferred into CD11c-YFP recipients, and recipients were immunized with CFA in the footpads. 18 h after T cell transfer and immunization, popliteal LNs were explanted and visualized by two-photon microscopy before and after the addition of SL8 peptide antigen. Imaging was performed in the most superficial 80 µm of the LN to replicate imaging conditions during TCR visualization. Data were pooled from four experiments. See Video 5 for representative video. For all data with antigen, time = 0 represents the time at which the antigen was added. (a) Representative tracks displaying cell paths during 10 min of imaging. (b) Mean T cell crawling velocity. (c) Duration of T cell arrest. (d) Duration of T cell-DC contact. (b-d) Statistical analysis was performed using a one-way analysis of variance with Tukey's post test. Each dot represents one cell, and the bars represent the mean.

occurred without motility arrest (Fig. 8 a). Data were combined from CFA-draining and nondraining LNs with no significant difference in the frequency or duration of TCR clustering. In the example shown, the T cell showed no consistent clustering of the TCR at the initial time point imaged, with a slight polarization toward the leading edge of the cell. However, at the 2–4 min time points, a clustering of the TCR was seen along the midzone region. By the 6 min time point, the TCR clustering had largely dissipated (Fig. 6 a and Fig. S3 a).

Naive T cells in the LN rapidly cluster their TCR in response to their first exposure to cognate antigen

Using the technique we established to synchronize antigen recognition primarily on DCs in the LN, we next analyzed

TCR dynamics in naive T cells during antigen recognition (Figs. 6 and 7). Within the 30 min after antigen addition, 47.6% of OT-I–GFP T cells arrested, as assessed by reduced crawling velocity and morphological rounding, and 36.6% of T cells showed transient or stable TCR clustering (Fig. 7, a–c). As we observed *in vitro*, detectable TCR clustering was short (7.1 ± 5.1 min), although significantly more sustained than TCR clustering in the absence of antigen (Fig. 7 d). Because of the brief nature of the antigen-dependent TCR clustering, the frequency of detectable TCR clustering declined within 30 min of antigen recognition (Fig. 7 a).

In the example shown (Fig. 6 b, Fig. S3 b, and Video 6), the T cell began to cluster its TCR 8 min after the addition of antigen, before morphological rounding. By 12 min after

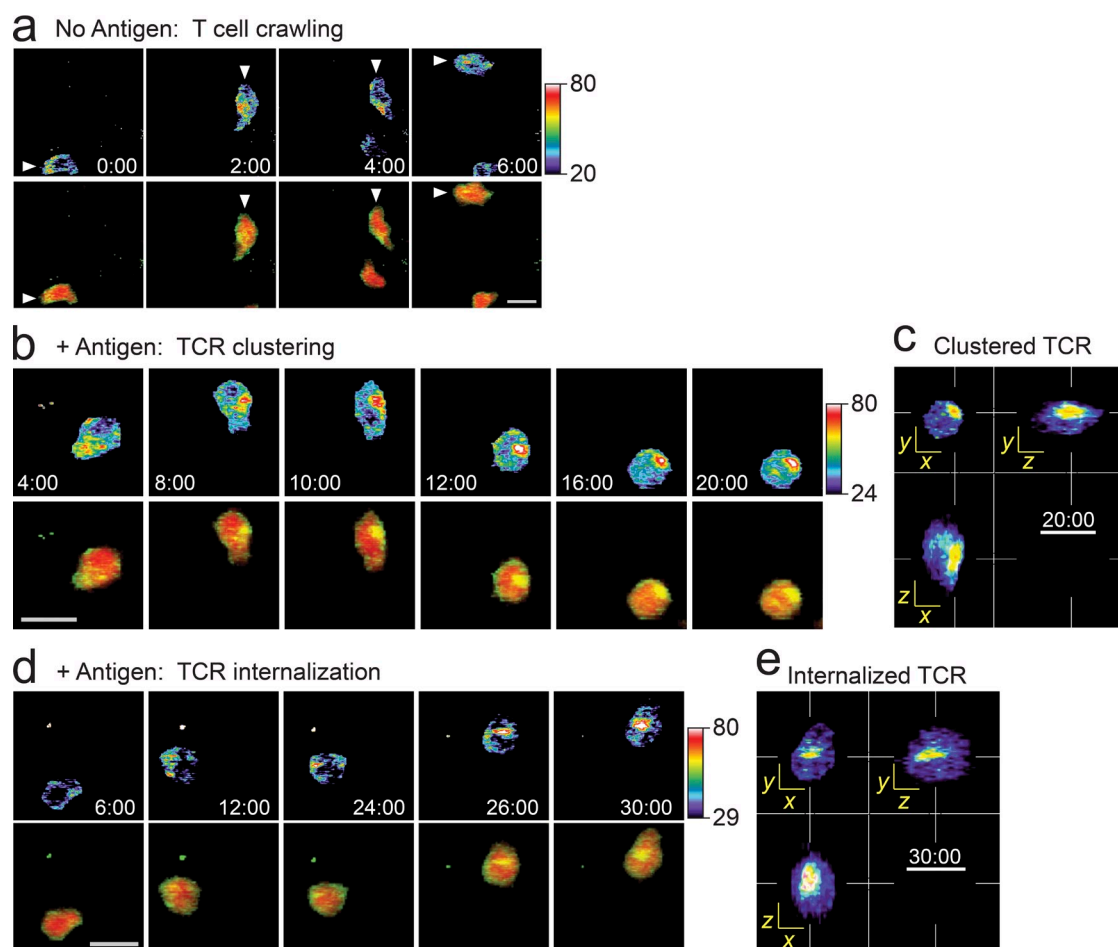


Figure 6. Rapid TCR clustering and internalization during the initial stages of antigen recognition. CMTMR-labeled OT-I–GFP Rag2^{-/-} cells were transferred into WT recipients and immunized as in Fig. 5. LNs were explanted and visualized by two-photon microscopy. Data are representative of more than five experiments. For all data with antigen, time = 0 represents the time at which the antigen was added. (a, b, and d) Maximum intensity z projections of OT-I–GFP fluorescence represented in pseudocolor (top) and overlaid OT-I–GFP fluorescence and CMTMR fluorescence in red (bottom). (a) Representative time-lapse image of OT-I–GFP TCR localization on a crawling T cell in a nondraining LN in the absence of antigen. White arrowheads indicate the leading edge of the cell of interest. Image was collected using the 510/20-nm filter. (b) Representative time lapse of sustained OT-I–GFP TCR clustering after antigen addition. Image was collected using the 525/50-nm filter. For full video, see Video 6. (c) TCR clustering associated with the cell surface. Orthogonal views of OT-I–GFP fluorescence of the T cell represented in b showing a 1.6 (x) × 1.6 (y) × 2- μ m (z) slice through the cell at the location indicated by the crosshairs. (d) Representative time lapse of OT-I–GFP TCR internalization after antigen addition. Image was collected using the 525/50-nm filter. For full video, see Video 7. (e) TCR internalization. Orthogonal views of OT-I–GFP fluorescence of the T cell represented in d showing a 1.6 (x) × 1.6 (y) × 2- μ m (z) slice through the cell at the location indicated by the crosshairs. Bars, 10 μ m.

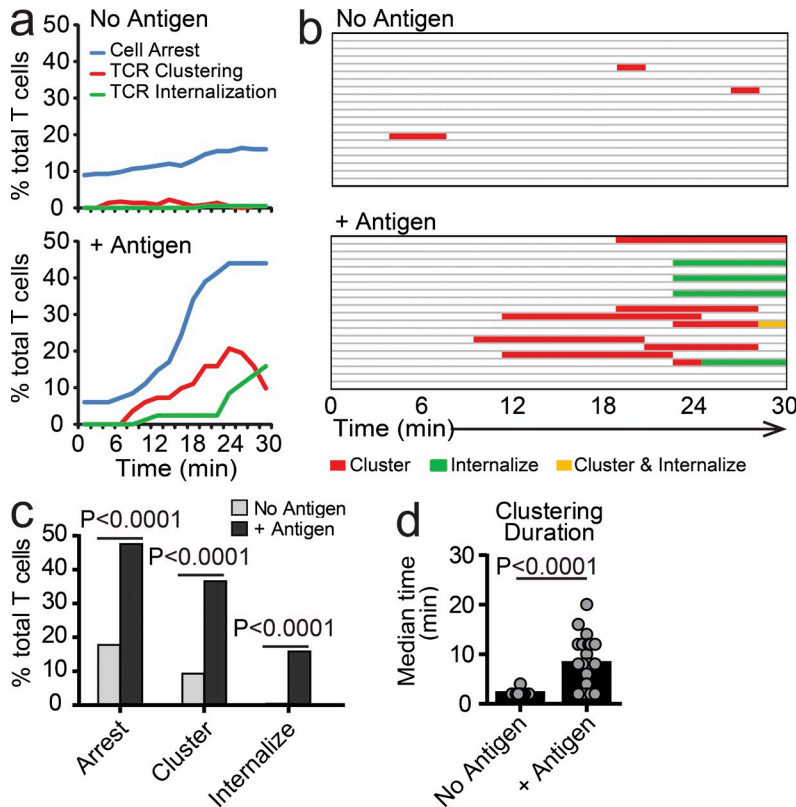


Figure 7. Transient antigen-independent TCR clustering and rapid antigen-dependent TCR clustering and internalization in vivo. CMTMR-labeled OT-I-GFP Rag2^{-/-} cells were transferred into WT recipients and immunized, and LNs were imaged by two-photon microscopy as in Figs. 5 and 6. Data analyzed were combined from images collected using the 510/20- and 525/50-nm filters. For all data with antigen, time = 0 represents the time at which the antigen was added. (a) Bulk dynamics of T cell motility arrest, TCR clustering, and TCR internalization in the presence and absence of antigen. For no antigen, $n = 225$ combined from four experiments. For + antigen, $n = 82$ combined from three experiments. (b) Dynamics of TCR clustering and TCR internalization in individual cells in the presence and absence of antigen. Each line corresponds to a single randomly selected representative cell. (c) Frequency of T cell motility arrest, TCR clustering, and TCR internalization. For no antigen, $n = 225$ combined from three experiments. For + antigen, $n = 82$ combined from three experiments. Statistical analysis was performed using Fisher's exact test. (d) Duration of TCR clustering. Only cells with clustered TCR are represented. Each dot represents one cell, and the bars represent the median. For no antigen, $n = 21$ combined from four experiments. For + antigen, $n = 30$ combined from three experiments. Statistical analysis was performed using a two-tailed t test with Welch's correction.

antigen addition, the T cell showed strong TCR clustering with arrest, as indicated by reduced crawling velocity and morphological rounding. Orthogonal slices through the cell showed that the TCR cluster was on or near the cell surface (Fig. 6 c and Fig. S3 b). Although our system was able to detect TCR clusters, we were unable to resolve TCR microclusters, which require resolution and detection efficiencies that are only amenable to *in vitro* imaging techniques such as total internal reflection fluorescence (TIRF) microscopy. For similar spatial resolution reasons, we were also unable to eliminate the possibility that some clusters were internalized, even when the fluorescence density appeared near the cell periphery.

Rapid TCR internalization in the LN does not require sustained TCR surface clustering

The decline of TCR surface clustering after antigen recognition was concurrent with an increase in TCR internalization (Fig. 7 a), with 15.9% of T cells showing clear evidence of TCR internalization (Fig. 7 c). In support of cSMAC-independent TCR internalization (Fig. 2 and Videos 3 and 9) occurring during early antigen recognition in the LN environment, TCR internalization was observed in some cases without detection of sustained TCR surface clustering (Fig. 7 b). In the example shown (Fig. 6 d, Fig. S3 c, and Video 7), the T cell showed morphological rounding and reduced velocity at 12 min after antigen addition without sustained TCR surface clustering. At 24 min after antigen addition, the T cell maintained the rounded morphology, and a low level of TCR clustering became visible. Within 2 min,

the TCR clusters quickly moved away from the cell surface toward the center of the cell, indicating bona fide internalization. During the course of TCR internalization, the T cell maintained low level motility in the absence of rounded morphology, indicating that the cell did not remain arrested. The TCR internalization was confirmed by orthogonal slices through the cell showing that the clusters were not associated with the cell surface (Fig. 6 e and Fig. S3 c).

Because there was a possibility of peptide being presented by non-DCs, we used a second approach to target antigen only to DCs. Using anti-DEC205:OVA and anti-CD40 immunization, we also observed frequent TCR internalization in the draining LN (Fig. S4 and Videos 11–13). In several cases, we observed TCR internalization before TCR clustering (Fig. S4 and Videos 11–13). In these cases, the surface clusters might have been derived from internalized vesicles of TCR trafficking to the T cell–DC interface. In this setting, it was difficult to track T cell motility because many T cells were found clustered around what were likely DCs. Although many cells were arrested, there was a significant amount of T cell motility within the clusters. This immunization system also supported rapid TCR internalization rather than clustering at a cSMAC-like structure.

TCR signaling is often associated with but is not dependent on motility arrest

In vitro, TCR clustering and internalization often occurred after a dramatic decrease in T cell velocity and establishment of rounded morphology (Fig. 2 c and Video 2). However,

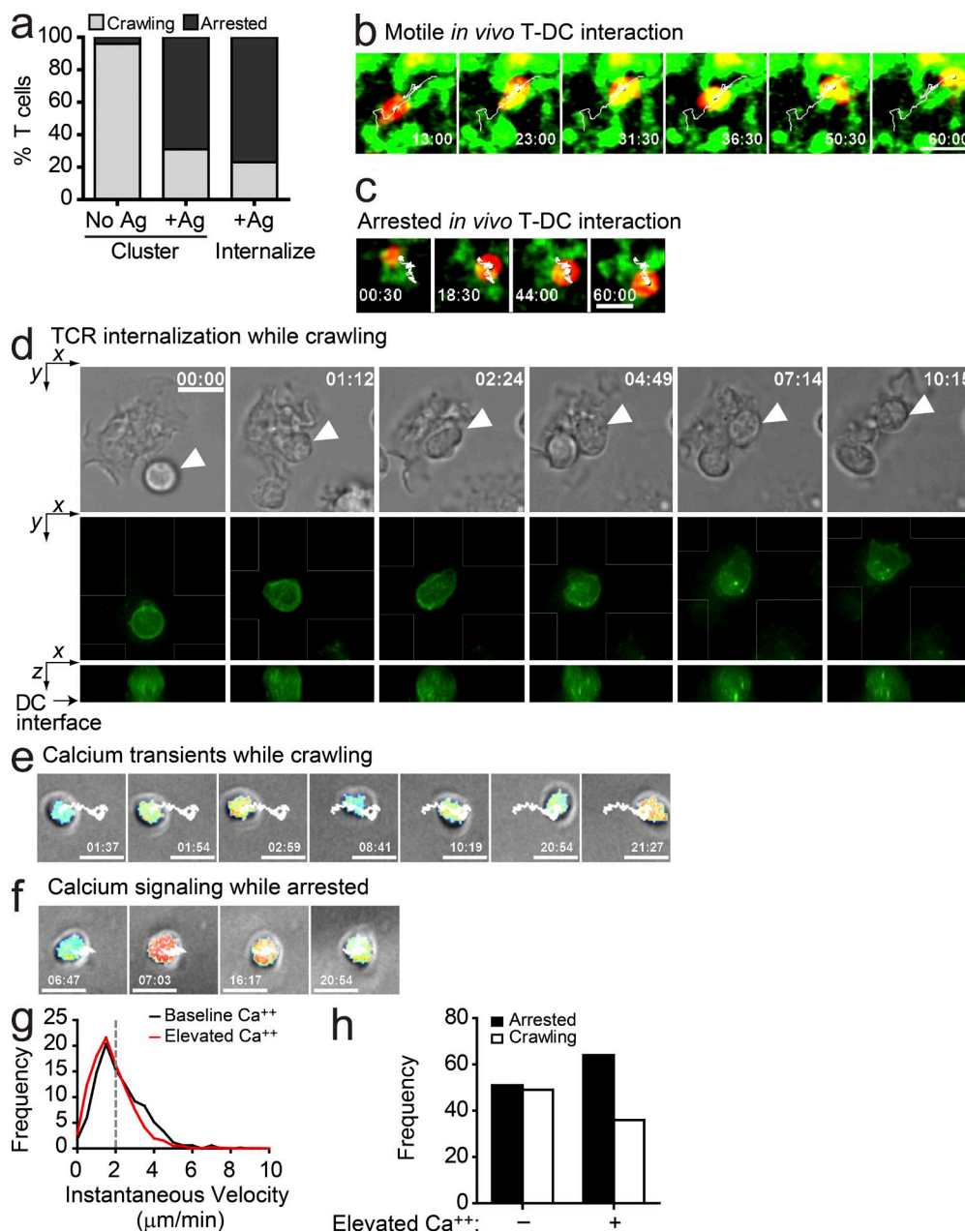


Figure 8. TCR signaling does not require motility arrest. (a–c) CMTMR-labeled OT-I-GFP Rag2^{-/-} cells were transferred into WT or CD11c-YFP recipients and immunized, and LNs were imaged by two-photon microscopy as in Figs. 5 and 6. (a) Contingency of TCR clustering and internalization on motility arrest *in vivo*. Only cells that clustered or internalized their TCR are represented. For clustering no antigen (Ag), $n = 21$ combined from four experiments. For clustering + antigen, $n = 30$. For internalization + antigen, $n = 13$ combined from three experiments. (b and c) Single z -plane time lapse images of *in vivo* T cell–DC interactions in the presence of antigen. See [Video 8](#) for the full time lapse. Data are representative of four experiments. (b) Motile *in vivo* T cell–DC interaction. (c) Arrested *in vivo* T cell–DC interaction. (d) Representative *in vitro* time lapse of a naive OT-I-GFP T cell internalizing TCR while crawling along an antigen-bearing DC. The T cell internalizes its TCR through microclusters as it maintains an active leading edge and continually crawls along a DC. Contrast (top) and maximum intensity z projection of OT-I-GFP fluorescence (bottom) are shown. Arrowheads point to the T cell of interest. The white lines define the xy space rendered in the xz rendering below. See [Video 9](#) for the full time lapse. (e–h) Naive OT-I T cells were labeled with Fura-2AM and placed on lipid bilayers presenting pMHC + ICAM-1. Data are representative of two experiments. (e and f) Contrast (grayscale background image) and calcium imaging (pseudocolor overlay) visualized by epifluorescence microscopy. Low–high calcium is represented by a blue–white pseudocolor scale. See [Video 10](#) for the full time lapses. (e) Representative time lapse of calcium signaling while crawling along a lipid bilayer with oscillations in calcium levels and motility. (f) Representative time lapse of a T cell fluxing calcium while arrested. (b, c, e, and f) White lines show cell tracks. (g and h) Quantification of motility with relation to calcium signaling. At each time point, the instantaneous velocity of the cell was correlated with its calcium level. Time points with a Fura-2AM 340-nm/380-nm emission ratio of $>1.4\times$ baseline were scored as having elevated calcium. Time points with an instantaneous velocity $<2 \mu\text{m}/\text{min}$ were scored as arrested. The dashed line indicates the cutoff value below which cells were termed nonmotile ($2 \mu\text{m}/\text{min}$). $n = 1,970$ time points from 40 cells pooled from two experiments. Bars: (b and d–f) $10 \mu\text{m}$; (c) $5 \mu\text{m}$.

arrest, as indicated by consistently reduced crawling speed ($<2 \mu\text{m}/\text{min}$) and morphological rounding, was not necessary for TCR clustering or internalization to occur (Fig. 8 a). In fact, in a subset of cells in vivo, full arrest did not occur or occurred up to 10 min after the initiation of TCR clustering or internalization (Fig. 6, b and d; Fig. 8 a; and Videos 6 and 7). We were unable to visualize the DCs during these motile signaling events in vivo. However, we previously observed that the DCs in the interfollicular ridges formed a relatively stationary network with very few motile cells (Video 5). Specific analysis of T cell–DC interactions compared with the paths of T cells (Fig. 8, b and c; and Video 8) strongly suggested that observed movement of the T cells in vivo was primarily attributable to the motility of the T cell and not the DC. These cells appear to be signaling while undergoing continued motility and shape changes. In addition, we observed the same motile signaling behavior in vitro during T cell interactions with DCs (Fig. 8 d and Videos 3 and 9). This is particularly evident in interactions exemplified by Fig. 8 d and Video 9 in which the T cell maintained a highly active lamellipodium and slowly crawled along the DC while internalizing its TCR in the absence of a cSMAC.

Because both in vitro and in vivo assays showed motile interactions that induced TCR signaling, we sought to use calcium imaging in vitro to further define motile T cell signaling. We measured T cell motility during calcium signaling on lipid bilayers presenting pMHC and ICAM-1 using naive OT-I T cells labeled with the calcium-sensitive dye Fura-2AM. We observed time periods during which T cells signaled in the arrested state and time periods during which T cells signaled while motile (Fig. 8, e–h; and Video 10). To analyze the correlation between calcium signaling and motility, we assessed the calcium levels and crawling velocity at each time point of each of the cells evaluated. When cells were grouped based on a threshold defining whether they had baseline or elevated ($>1.4\times$ baseline) calcium levels, we found little difference in the instantaneous velocities between the two groups (Fig. 8 g). When we set a threshold for motility of $2 \mu\text{m}/\text{min}$ as we had for our in vivo analyses, there was a higher frequency of cells that were arrested during periods of elevated calcium, but nonetheless, 35% of cells with elevated calcium also moved at speeds $>2 \mu\text{m}/\text{min}$. Collectively, these results demonstrate that in naive T cells, contacts leading to rapid TCR clustering, TCR internalization, and calcium signaling are often associated with but not contingent upon motility arrest and that naive T cells are able to integrate signaling and motility.

DISCUSSION

The data presented in this study are a first view of synapses as they occur in naive cells in vivo. The fundamental findings are threefold. First, prolonged TCR clustering or cSMAC formation for naive T cells interacting with DCs was infrequent in vivo as well as in vitro. Second, TCR internalization can occur rapidly in the absence of stable cSMAC formation. Finally, T cells are able to actively aggregate TCRs, flux calcium, and internalize TCR clusters, even in a motile synapse.

These data create the need to reconsider the dichotomy between T cell migration versus TCR clustering and signaling as clearly they are not exclusive. In our opinion, there is a spectrum of behaviors associated with signaling that does not require the stability of a synapse. These behaviors include calcium influx and formation and internalization of TCR clusters. This is somewhat at odds with older studies that suggested that calcium signaling and TCR occupancy necessarily led to arrest (Negulescu et al., 1996; Dustin et al., 1997) but likely could be reconciled if one considers that some of those studies may have used conditions of stimulation or cell lines that were more sensitive to motility arrest and that the speed of migration does decrease, even in cells that maintain motility. Another factor that may play into differences is that our analysis of TCR dynamics in naive T cells was limited to CD8 T cells expressing a high affinity TCR. As a result, it is difficult to assess the universality of our results for other TCRs or for CD4 T cells versus CD8 T cells. However, the fact that we saw very similar results over a 2-log range of antigen doses and after in vivo immunization suggests that this effect is not limited to superphysiological antigen levels or conditions uniquely present in vitro.

The idea that synapses can be motile fits well with a body of emerging data suggesting that cells can signal while moving. The first evidence for this was observations of T cell activation by motile interactions with DCs in collagen matrices (Gunzer et al., 2000). Subsequently, a series of in vivo observations in LNs provided evidence of early signaling resulting in CD69 up-regulation, T cell proliferation, and cytokine production after short-lived encounters (Mempel et al., 2004; Miller et al., 2004; Celli et al., 2005). Recently, Dustin (2007) has suggested the term kinapse to differentiate motile synapses from the stable cSMAC/peripheral SMAC-containing immunological synapse (Monks et al., 1998; Grakoui et al., 1999). Based on our data, it is notable that the appearance of signaling clusters, calcium influx, and synapse formation (tight membrane apposition) are similar under motile and nonmotile conditions and likely represent a continuum of signaling modes rather than a strict dichotomy. A likely reason for very highly stabilized membrane–membrane junctions leading to symmetrical cSMAC structures could be that in homogenous systems such as lipid bilayers or B cell APCs, T cells receive symmetrically equivalent signals from all borders of the synapse, so actomyosin-based motility is balanced inward toward the center of the cSMAC. In that regard, PKC- θ -deficient T cells appear to lack this balance and are highly motile, even on bilayer substrates (Sims et al., 2007). Bilayers and some APCs may create an abnormally large tight apposition between the T cell and APC, whereas T cell–DC junctions are more typically multifocal (for review see Doh and Krummel, 2010). Such tight apposition might disfavor continued migration and allow assembly of a single large synapse structure that restricts remodeling and allows formation of highly localized internalization domains.

The brief nature of TCR clustering that we observed in naive cells in multiple settings is likely related to rapid TCR

internalization. Because TCR internalization and downmodulation is a direct result of TCR signaling (Valitutti et al., 1997; Liu et al., 2000), the presence of TCR clustering and internalization provides perhaps the first direct evidence for TCR signaling by naive cells in the early and transient interactions after antigen recognition *in vivo*. It should be noted that we were unable to distinguish between surface clustering and internalized TCR just below the membrane because of the resolution of the imaging techniques used. As a result, there is a possibility that we overestimated the frequency and stability of surface cSMACs and underestimated the frequency and speed of internalization.

Based on several *in vitro* studies, it has been inferred that the cSMAC is likely to be the site of TCR internalization (Lee et al., 2003; Varma et al., 2006; Vardhana et al., 2010); however, the spatiotemporal dynamics of these events have not previously been examined. Although in some cases we did observe TCR internalization occurring from the site of stable TCR surface clustering, in others, TCRs were internalized in the absence of detectable, stable, and prolonged surface clustering. In these cases, internalization likely occurred from sites of TCR microclusters that were below our limit of detection or after rapid aggregation of these microclusters at speeds faster than our rate of acquisition (2 min/frame). Based on these data demonstrating variability of the site of internalization, it will be interesting to see whether the mechanisms of TCR downmodulation and signal termination observed in the cSMACs of activated cells stimulated by passive antigen-presenting surfaces are also used by naive T cells stimulated by DCs. It is likely that in these settings, recruitment of LBPA would be more multifocal with heterogeneity of signal termination among microclusters in the same cell.

The overall motility seen during TCR signaling was slow, as would be expected during a motile interaction in which a T cell crawls along the surface of a DC or a network of DCs. In fact, TCR signaling inactivates the contractile machinery necessary for rapid motility by phosphorylating myosin IIA (Jacobelli et al., 2004). Upon myosin IIA inhibition or depletion, T cells maintain an active lamellipodium and slide along in a slow, actin protrusion-dependent mode of motility (Jacobelli et al., 2009). This mode of slow motility during TCR signaling might serve to ensure that the T cell can detect and integrate as many antigen signals as possible by probing as large of an antigen-presenting surface as possible.

Our *in vivo* imaging of TCR dynamics in the absence of cognate antigen showed transient clustering of the TCR without discernable T cell arrest or rounded morphology. We observed these clustering events at low frequencies, and they were much more transient than reports of antigen-independent receptor clustering observed *in vitro* (Revy et al., 2001), likely caused by the three-dimensional environment in the LN. Our imaging was performed in regions of the T cell zone containing an extensive DC network, providing frequent access for antigen-independent interactions. Clustering events such as these may be stochastic, representing a contact with specialized APCs, or might be a random

membrane dynamic that is independent of TCR engagement. An intriguing possibility is that *in vivo*, these result from interactions with eTACs (extra-thymic Aire-expressing cells) presenting self-antigens (Gardner et al., 2008). Notably, eTACs are clustered in the interfollicular regions of the T zone in the LN, where we imaged the TCR.

The image acquisition and processing strategies we developed in this study have allowed us to analyze surface and intracellular TCR dynamics in naive cells in the LN for the first time by enhancing detection and discrimination of *in vivo* fluorescent signals. It is clear that the use of fluorescent probes that read out more than cellular positioning are the next hurdle to gain further insight from real-time analyses of cells *in situ*. The method we have described is significant in that it will allow for the *in vivo* analysis of the dynamics of other signaling molecules using fluorescent reporters, even when expressed at physiologically appropriate levels. This, in turn, will allow increased understanding of receptor and signaling dynamics within single cells in real time and in their native environments.

The development of real-time molecular imaging *in situ* has provided us with a view of TCR dynamics that represent the complexities of physiological interactions, including observations of motile signaling modes that might allow for optimal scanning of the T cell's environment. Continued evolution of these imaging and analysis methods will help integrate signaling dynamics into the biology of complex systems.

MATERIALS AND METHODS

OT-I-GFP transgenic construct and mice

We chose to GFP tag the OT-I TCR, which is specific for the chicken egg OVA-derived SIINFEKL peptide (SL8) in the context of the MHC class I molecule H2-k^b, because it is well characterized and a variety of tools exist to facilitate its use. We obtained the original OT-I transgenic constructs from F. Carbone (University of Melbourne, Melbourne, Victoria, Australia; Hogquist et al., 1994). The OT-I- α chain was tagged on the C terminus with a 20-aa flexible linker and a single enhanced GFP (Takara Bio Inc.) using standard molecular cloning techniques and was expressed under the CD4 enhancer and promoter without the silencer (Sawada et al., 1994). The OT-I- β chain was expressed under its endogenous promoter (Hogquist et al., 1994). The transgenic constructs were injected directly into C57BL/6 oocytes by the University of California, San Francisco Transgenic Core Facility, and founders were screened by expression of the V α 2 and V β 5 TCR chains as well as GFP positivity. C57BL/6 mice were purchased from The Jackson Laboratory or Simonsen Services. Actin-CFP, CD11c-YFP, and OT-I mice were bred in-house. Experimental procedures were approved by and mice were handled in accordance with the guidelines of the University of California, San Francisco Institutional Animal Care and Use Committee.

Reagents, antibodies, and flow cytometry

Anti-V α 2 (clone B20.1), anti-V β 5 (clone MR9.4), anti-MHC class II (clone N22), anti-MHC class I (clone 5F1), and anti-DEC205 (clone NLDC-145) antibodies were made in-house. Anti-V α 2 and anti-MHC class II were conjugated with RPE (Prozyme), and anti-V β 5 and anti-MHC class I were conjugated with Alexa Fluor 647 (Invitrogen). Anti-CD4 Alexa Fluor 647, anti-CD8 Alexa Fluor 647, and anti-CD16/CD32 (24G.2) antibodies were made by the University of California, San Francisco Hybridoma Core Facility. Anti-B220 PerCP, anti-CD4 PerCP, anti-CD8 PerCP, anti-CD11c PE, anti-CD19 APC, anti-CD40 PE, anti-ICAM-1 FITC, and streptavidin APC were purchased from BD. Anti-CD11c biotin and anti-CD40 were purchased from eBioscience. SL8 (OVA 257–264) peptide was purchased from AnaSpec, and maleimide-activated OVA protein was purchased

from Thermo Fisher Scientific. LNs were dissociated or digested with collagenase D (Roche) and then dissociated. Single cell suspensions were blocked with 24G.2 and stained. Samples were acquired on a FACSCalibur (BD) and analyzed using FlowJo (Tree Star, Inc.).

Cell selections and labeling

CD8⁺ T cells were enriched from LNs and spleens using the StemSep CD8 T cell negative selection kit (STEMCELL Technologies Inc.). T cells were either left unlabeled or labeled with 20 μ M CMTMR (Invitrogen) or 2.5 μ M CFSE (Invitrogen) as indicated.

Lipid bilayers

Small unilamellar vesicles consisting of 96.5% POPC, 2% DGS-NTA-Ni, 1% Biotinyl-CAP-PE, and 0.5% PEG5,000-PE were prepared by rehydrating dried phospholipid cakes into PBS and extruding through 100-nm pore-size filters using a LiposoFast extruder (Avestin). Lipid bilayers on glass were blocked with 1% BSA, loaded with 5 μ g/ml streptavidin, and then loaded with 12 \times his-ICAM and biotinylated pMHC (SIINFEKL-loaded H2-k^b).

TIRF and calcium flux microscopy

Naive WT OT-I CD8⁺ T cells and OT-I-GFP CD8⁺ T cells were surface labeled for the TCR- β chain using H57-Alexa Fluor 568. The TIRF microscope described previously (Jacobelli et al., 2009) was modified to include an electron-multiplying charge-coupled device (Evolve; Roper Industries), ASI-MS200 stage (Applied Scientific Instrumentation), and 100 \times NA 1.46 Plan-Apochromat objective. OT-I-GFP and antibody-labeled TCR images were acquired in TIRF mode with 100-ms exposures at 1-s intervals. For calcium release imaging on bilayers, epifluorescent illumination was performed using a DG4 (Sutter Instrument Co.) with 340- and 380-nm filters. Cells were loaded with 1 μ M Fura-2AM and imaged at 15-s intervals beginning \sim 1 min after cells began interacting with the bilayer.

Proliferation

Naive CFSE-labeled OT-I-GFP CD8⁺ T cells and WT OT-I CD45.1⁺ CD8⁺ T cells were cotransferred intravenously through the tail vein into C57BL/6 recipients. Immediately after cell transfer, recipient mice were immunized subcutaneously in the flanks with CFA (Difco) emulsified with SL8 peptide at the indicated concentration. Draining inguinal LNs were harvested 66 h after transfer and immunization. CFSE dilution was analyzed by flow cytometry. OT-I CD45.1⁺ T cells and OT-I-GFP T cells were identified by the expression of CFSE, V α 2, and V β 5 and distinguished from each other based on CD45.1 expression.

TCR down-regulation

Bone marrow-derived DCs were pulsed with the indicated concentration of SL8 peptide and then washed three times. DCs were combined with naive CD8⁺ OT-I-GFP T cells or naive WT CD8⁺ OT-I T cells. Cells were immediately centrifuged for 1 min at 228 g and were incubated at 37°C for the indicated amount of time. After incubation, cold PBS (Invitrogen) + 4 mM EDTA (Sigma-Aldrich) was added, and cells were pipetted and placed on ice to disrupt the T cell-DC couples. Cells were stained with anti-CD8 to identify T cells, anti-V β 5 to identify OT-I and OT-I-GFP T cells as well as to measure surface TCR expression, and anti-MHC class II to gate out DCs. Cells were analyzed by flow cytometry. Percent surface TCR surface expression was calculated from the mean fluorescent intensity of V β 5 staining and normalized based on the mean fluorescent intensity at the zero time point.

Flow cytometry-based coupling

Bone marrow-derived DCs were pulsed with the indicated concentration of SL8 peptide and then washed three times. DCs were combined with naive CD8⁺ OT-I-GFP T cells or naive WT CD8⁺ OT-I T cells. Cells were immediately centrifuged for 1 min at 228 g and were incubated at 37°C for the indicated amount of time. After incubation, cells were vortexed and fixed for 10 min at 37°C with warm 2% paraformaldehyde (Electron Microscopy Sciences) in PBS and were washed. Cells were stained to identify DCs

(anti-MHC class II) and T cells (anti-CD8) and analyzed by flow cytometry. The percentage of couple formation was calculated as the number of T cells in the double-positive quadrant (CD8⁺ MHC class II⁺) versus the total number of T cells (CD8⁺).

Cytotoxicity assays

WT OT-I and OT-I-GFP LN cells were stimulated in vitro with 100 ng/ml SL8 peptide-pulsed splenocytes. 5 d after activation, the T cells were used in a standard 4-h ⁵¹Cr release cytotoxicity assay using ⁵¹Cr (PerkinElmer)-labeled EL-4 cells as targets either pulsed with 100 ng/ml SL8 peptide or left unpulsed.

Epifluorescence microscopy

A modified microscope (Axiovert 200M; Carl Zeiss, Inc.) with Plan-Neofluar 40 \times and 60 \times objectives (Carl Zeiss, Inc.) was used for epifluorescence imaging experiments. The microscope was fitted with dual excitation and emission filter wheels and a camera (CoolSNAP-HQ; Photometrics). The imaging and control software used was MetaMorph (MDS Analytical Technologies). For imaging of TCR dynamics, bone marrow-derived DCs were pulsed with the indicated concentration of SL8 peptide and then washed three times. The DCs were plated with naive CD8⁺ OT-I-GFP T cells or CD8⁺ OT-I-GFP T cell blasts in chamber slides (Nunc) in RPMI medium without phenol red (Invitrogen) containing 10% FBS (HyClone) and 0.25% low-melting-point agarose (BMA). Cells were incubated for 10 min at 37°C before imaging and were maintained at 37°C on the heated stage of the microscope. Data from differential interference contrast images and GFP fluorescence were collected at 30-s intervals over a 15–30-min period. Only T cells that contacted DCs were scored. Cells with synapses were identified as having a tight interface between the T cell and DC membranes. cSMACs were characterized as central accumulations of the TCR at the T cell-DC interface. Internalized TCR was characterized as vesicles within the T cell that were not attached to the T cell membrane.

Two-photon microscopy

LN preparation. For all conditions, explanted LNs were immobilized on coverslips with the efferent lymphatics adhered to the coverslip. The interfollicular areas of the T zone in the most superficial 80 μ m of the LNs were imaged through the cortical side of the LN. During imaging, LNs were maintained at 35.5–37°C in a flow chamber perfused with RPMI medium without phenol red saturated with 95% O₂/5% CO₂.

For imaging the OT-I-GFP TCR, LN cells and splenocytes from OT-I-GFP Rag2^{-/-} mice were labeled with 20 μ M CMTMR, washed three times, and transferred intravenously through the tail vein into C57BL/6 recipients. For imaging the cellular dynamics of OT-I-GFP Rag2^{-/-} and polyclonal CD8 T cells, CD8⁺ T cells selected from actin-CFP mice were cotransferred with CMTMR-labeled OT-I-GFP Rag2^{-/-} cells into CD11c-YFP recipients. Immediately after cell transfer, recipients were immunized subcutaneously in the footpads with CFA emulsified with PBS. 18 h after immunization and T cell transfer, the mice were sacrificed, and their draining popliteal LNs and the nondraining maxillofacial LNs were surgically removed for imaging. Antigen-independent TCR dynamics were analyzed in both the draining popliteal and nondraining maxillofacial LNs. For analysis of the T cell response to cognate antigen, 100 ng/ml SL8 peptide was added to the media perfusing the draining popliteal LN. For all data reported after antigen addition, the beginning of the elapsed time reported denotes the time of antigen addition.

For imaging TCR dynamics after anti-DEC205:OVA immunization, WT C57BL/6 mice were immunized in each of the footpads with 5 μ g OVA-conjugated anti-DEC205 and 10 μ g anti-CD40 (clone 1C10). 18 h after immunization, CMTMR-labeled OT-I-GFP Rag2^{-/-} cells were transferred into the immunized recipients. 4 h after T cell transfer, mice were sacrificed, and the draining popliteal LNs were surgically removed for imaging.

Imaging instrumentation and conditions. For two-photon imaging, we used custom resonant-scanning instruments based on published designs containing a four-PMT array operating at video rate (Bullen et al., 2009). A custom four-dimensional acquisition module in the Video Savant digital

video recording software (IO Industries) was used for image acquisition (Bullen, et al., 2009). For imaging the OT-I-GFP TCR, samples were excited with a 5-W MaiTai Ti:Sapphire laser (Spectra-Physics) tuned to a wavelength of 910 nm and fitted with a FemtoControl pulse compressor (APE). The following dichroics and filters were used for blue, green, and red emission channel acquisition. For detection of second harmonic generation in the blue channel, a 495-nm LP dichroic and 455–485-nm bandpass emission filter were used. For detection of GFP in the green channel, a 560-nm LP dichroic and 500–500- or 500–520-nm bandpass emission filter were used. For detection of CMTMR in the red channel, the emission passing the previous dichroic was filtered using a 567–640-nm bandpass. All filters and dichroics were purchased from Chroma Technology Corp. To improve detection of GFP⁺ cells, the green channel was collected using a high-gain GaAs PMT module (H7422P; Hamamatsu Photonics). All other channels were collected using R5929 PMT modules (Hamamatsu Photonics). Images were collected using standardized PMT and laser power settings. For time-lapse image acquisition, each xy plane spanned 192 × 160 μm at a resolution of 0.40 μm/pixel. 60 frames collected at video rate were averaged, giving effective collection times of ~2 s per plane. Images of up to 50 xy planes with 1-μm z spacing were acquired every 2 min for 30 min.

For imaging the cellular dynamics of OT-I-GFP and polyclonal T cells, samples were excited with a 10-W MaiTai Ti:Sapphire laser tuned to a wavelength of 880 nm. Emission wavelengths of 455–485 (for CFP; blue), 500–550 (for YFP; yellow), and 567–640 nm (for CMTMR; red) were collected using R5929 PMT modules. For time-lapse image acquisition, each xy plane spanned 206 × 172 μm at a resolution of 0.43 μm/pixel. 20 frames collected at video rate were averaged, giving effective collection times of ~0.66 s per plane. Images of up to 30 xy planes with 3-μm z spacing were acquired every 30 s for 60 min. Experiments imaging the TCR dynamics in response to anti-DEC205:OVA immunization were performed using the exclusive “M” microscope (FV1000MPE; Olympus) with a XLPLN25XWMP super 25× NA 1.05 water immersion objective and a Mai-Tai HP DeepSee-OL laser (Spectra-Physics).

Data analysis. Data were visualized and analyzed using Imaris (Bitplane AG), MATLAB (MathWorks), and MetaMorph software. Statistical analysis was performed using Prism software (GraphPad Software, Inc.).

Analysis of cellular and TCR dynamics. Individual cells were identified and tracked by Imaris, and cellular velocity was calculated from tracks. T cell-DC interactions and T cell arrest were manually scored, aided by tracks generated by Imaris to identify cell paths. T cell arrest was defined as moving less than one cell body’s distance and showing morphological rounding for a minimum of 4 min (approximately <2 μm/min). Only cells that were trackable for at least 10 min were included in the analyses. After image processing using linear unmixing and volumetric masking, TCR clustering and internalization were manually scored, aided by tracks generated by Imaris to identify cell paths. Clustering was scored as a clear punctate accumulation of TCR associated with the cell surface. Internalization was scored as an accumulation of TCR that was clearly not associated with the cell surface. Because of the resolution of our imaging, we cannot exclude the possibility that cells scored as positive for clustering had internalized vesicles of TCR that were closely associated with the membrane. If clustering or internalization of the TCR was ambiguous, the cell was scored as negative.

Linear unmixing. CMTMR-labeled WT OT-I cells in the LN were identified based on fluorescence in the red channel. In MetaMorph, a region was drawn around the medial z plane of each cell, and the mean fluorescence intensity in the green and red channels was recorded. The mean fluorescence intensity of each cell in the red and green channels was plotted, and a linear equation was fit to the data points. For example, for Fig. 4 d, 525/50-nm filter: $y = 0.3955x - 4.0856$ and $R^2 = 0.8566$; and 510/20-nm filter: $y = 0.0468x - 0.4865$ and $R^2 = 0.7045$ (Olympus scope: $y = 0.1074x + 121.89$ and $R^2 = 0.7528$).

Using MATLAB and the ImarisXT Image Arithmetic function, the contribution of the CMTMR fluorescence in the green channel was removed using the equations determined. For example, for Fig. 4 (e and f),

525/50-nm filter: corrected GFP = green - (0.3955 × red - 4.0856); and 510/20-nm filter: corrected GFP = green - (0.0468 × red - 0.4865). Background contributed by electrical noise and environmental light, measured in regions of the image that did not contain tissue, was then subtracted from the resulting image in the green channel.

Volumetric masking. A binary mask was created from the bright CMTMR voxel intensities (>50 counts for images acquired on the custom instrument). The GFP image was multiplied by this binary mask to create a masked GFP image, eliminating regions of green fluorescence and dim red fluorescence intensity (<50 counts for images acquired on the custom two-photon instrument).

Localized active contour segmentation. Because of the nonuniform background fluorescence of the LN and the heterogeneous distribution of TCR-GFP molecules within OT-I-GFP T cells, a segmentation algorithm capable of discriminating background from foreground pixels using local intensities was needed. A localized active contour algorithm (Lankton and Tannenbaum, 2008) was used to iteratively conform an initial binary mask to the edges of TCR-GFP volumes. Initial masks were created by masking CMTMR images with a threshold of <50 counts. Extraneous foreground pixels in initial masks associated with background fluorescence or neighboring T cells were removed, and the initial mask was iteratively deformed using the localized segmentation algorithm. Voxels from the interior of the mask were set to zero to create a cell surface mask. The membrane-localized TCR-GFP intensities were then calculated from the corrected GFP images using the cell surface mask. All analysis was performed in MATLAB with Image Processing Toolbox functions. The localized active contour algorithm was obtained from S. Lankton (Georgia Institute of Technology, Atlanta, GA).

Online supplemental material

Fig. S1 shows T cell-DC coupling and cytotoxicity of WT OT-I versus OT-I-GFP T cells. Fig. S2 shows the phenotype of DCs in the draining LN ±CFA immunization. Fig. S3 shows orthogonal slices of the images shown in Fig. 6 at all time points. Fig. S4 shows images of TCR internalization and clustering in the draining LN after targeted delivery of antigen to the DCs through immunization with anti-DEC205:OVA + anti-CD40. Videos 1–3 show full time-lapse videos of the images in Fig. 1 c and Fig. 2 (c and d), respectively. Video 4 shows a three-dimensional reconstruction of the images shown in Fig. 4 f. Video 5 shows a representative time-lapse video of data analyzed in Fig. 5. Videos 6 and 7 show full time-lapse videos of the images in Fig. 6 (b and c, respectively). Videos 8–10 show full time-lapse videos of the images in Fig. 8 (b–f). Videos 11–13 show full time-lapse videos of the images in Fig. S4 (a–c, respectively). Online supplemental material is available at <http://www.jem.org/cgi/content/full/jem.20091201/DC1>.

We thank F. Carbone for providing OT-I transgenic constructs, N. Killeen and the University of California, San Francisco Transgenic Facility for mouse generation, S. Lankton for the contour algorithm, S. Peck and the Biological Imaging Development Center for microscope care, S. Smith for assistance with the Olympus microscope, and J. Cyster, M. Miller, A. Boissonnas, and members of the Krummel laboratory for helpful discussions.

This work was supported by the Larry L. Hillblom Foundation (R.S. Friedman), the Cancer Research Institute (P. Beemiller), the National Institutes of Health (1R21RR024895), the Sandler Family Foundation, and the University of California, San Francisco Comprehensive Cancer Center Stewart Trust Cancer Research Award.

The authors have no competing financial interests.

Submitted: 2 June 2009

Accepted: 29 September 2010

REFERENCES

- Azar, G.A., F. Lemaître, E.A. Robey, and P. Bousso. 2010. Subcellular dynamics of T cell immunological synapses and kinapses in lymph nodes. *Proc. Natl. Acad. Sci. USA.* 107:3675–3680. doi:10.1073/pnas.0905901107
- Barcia, C., C.E. Thomas, J.F. Curtin, G.D. King, K. Wawrowsky, M. Candolfi, W.D. Xiong, C. Liu, K. Kroeger, O. Boyer, et al. 2006.

- In vivo mature immunological synapses forming SMACs mediate clearance of virally infected astrocytes from the brain. *J. Exp. Med.* 203:2095–2107. doi:10.1084/jem.20060420
- Bonifaz, L.C., D.P. Bonnyay, A. Charalambous, D.I. Darguste, S. Fujii, H. Soares, M.K. Brimnes, B. Moltedo, T.M. Moran, and R.M. Steinman. 2004. In vivo targeting of antigens to maturing dendritic cells via the DEC-205 receptor improves T cell vaccination. *J. Exp. Med.* 199:815–824. doi:10.1084/jem.20032220
- Bouso, P., and E. Robey. 2003. Dynamics of CD8+ T cell priming by dendritic cells in intact lymph nodes. *Nat. Immunol.* 4:579–585. doi:10.1038/ni928
- Brossard, C., V. Feuillet, A. Schmitt, C. Randriamampita, M. Romao, G. Raposo, and A. Trautmann. 2005. Multifocal structure of the T cell - dendritic cell synapse. *Eur. J. Immunol.* 35:1741–1753. doi:10.1002/eji.200425857
- Bullen, A., R.S. Friedman, and M.F. Krummel. 2009. Two-photon imaging of the immune system: a custom technology platform for high-speed, multicolor tissue imaging of immune responses. In *Visualizing Immunity. Current Topics in Microbiology and Immunology*. Vol. 334. D. McGavern and M. Dustin, editors. Springer, New York. 1–30.
- Celli, S., Z. Garcia, and P. Bouso. 2005. CD4 T cells integrate signals delivered during successive DC encounters in vivo. *J. Exp. Med.* 202:1271–1278. doi:10.1084/jem.20051018
- Cemerski, S., and A. Shaw. 2006. Immune synapses in T-cell activation. *Curr. Opin. Immunol.* 18:298–304. doi:10.1016/j.coi.2006.03.011
- Doh, J., and M.F. Krummel. 2010. Immunological synapses within context: patterns of cell-cell communication and their application in T-T interactions. *Curr. Top. Microbiol. Immunol.* 340:25–50. doi:10.1007/978-3-642-03858-7_2
- Dustin, M.L. 2007. Cell adhesion molecules and actin cytoskeleton at immune synapses and kinapses. *Curr. Opin. Cell Biol.* 19:529–533. doi:10.1016/j.ccb.2007.08.003
- Dustin, M.L., S.K. Bromley, Z. Kan, D.A. Peterson, and E.R. Unanue. 1997. Antigen receptor engagement delivers a stop signal to migrating T lymphocytes. *Proc. Natl. Acad. Sci. USA.* 94:3909–3913. doi:10.1073/pnas.94.8.3909
- Dustin, M.L., S.Y. Tseng, R. Varma, and G. Campi. 2006. T cell-dendritic cell immunological synapses. *Curr. Opin. Immunol.* 18:512–516. doi:10.1016/j.coi.2006.05.017
- Gardner, J.M., J.J. Devoss, R.S. Friedman, D.J. Wong, Y.X. Tan, X. Zhou, K.P. Johannes, M.A. Su, H.Y. Chang, M.F. Krummel, and M.S. Anderson. 2008. Deletional tolerance mediated by extrathymic Aire-expressing cells. *Science.* 321:843–847. doi:10.1126/science.1159407
- Grakoui, A., S.K. Bromley, C. Sumen, M.M. Davis, A.S. Shaw, P.M. Allen, and M.L. Dustin. 1999. The immunological synapse: a molecular machine controlling T cell activation. *Science.* 285:221–227. doi:10.1126/science.285.5425.221
- Gunzer, M., A. Schäfer, S. Borgmann, S. Grabbe, K.S. Zänker, E.B. Bröcker, E. Kämpgen, and P. Friedl. 2000. Antigen presentation in extracellular matrix: interactions of T cells with dendritic cells are dynamic, short lived, and sequential. *Immunity.* 13:323–332. doi:10.1016/S1074-7613(00)00032-7
- Hemmer, B., I. Stefanova, M. Vergelli, R.N. Germain, and R. Martin. 1998. Relationships among TCR ligand potency, thresholds for effector function elicitation, and the quality of early signaling events in human T cells. *J. Immunol.* 160:5807–5814.
- Hogquist, K.A., S.C. Jameson, W.R. Heath, J.L. Howard, M.J. Bevan, and F.R. Carbone. 1994. T cell receptor antagonist peptides induce positive selection. *Cell.* 76:17–27. doi:10.1016/0092-8674(94)90169-4
- Hugues, S., L. Fetler, L. Bonifaz, J. Helft, F. Amblard, and S. Amigorena. 2004. Distinct T cell dynamics in lymph nodes during the induction of tolerance and immunity. *Nat. Immunol.* 5:1235–1242. doi:10.1038/ni1134
- Hurez, V., A. Saparov, A. Tousson, M.J. Fuller, T. Kubo, J. Oliver, B.T. Weaver, and C.T. Weaver. 2003. Restricted clonal expression of IL-2 by naive T cells reflects differential dynamic interactions with dendritic cells. *J. Exp. Med.* 198:123–132. doi:10.1084/jem.20022230
- Itoh, Y., B. Hemmer, R. Martin, and R.N. Germain. 1999. Serial TCR engagement and down-modulation by peptide:MHC molecule ligands: relationship to the quality of individual TCR signaling events. *J. Immunol.* 162:2073–2080.
- Jacobelli, J., S.A. Chmura, D.B. Buxton, M.M. Davis, and M.F. Krummel. 2004. A single class II myosin modulates T cell motility and stopping, but not synapse formation. *Nat. Immunol.* 5:531–538. doi:10.1038/ni1065
- Jacobelli, J., F.C. Bennett, P. Pandurangi, A.J. Tooley, and M.F. Krummel. 2009. Myosin-IIA and ICAM-1 regulate the interchange between two distinct modes of T cell migration. *J. Immunol.* 182:2041–2050. doi:10.4049/jimmunol.0803267
- Jontes, J.D., M.R. Emond, and S.J. Smith. 2004. In vivo trafficking and targeting of N-cadherin to nascent presynaptic terminals. *J. Neurosci.* 24:9027–9034. doi:10.1523/JNEUROSCI.5399-04.2004
- Khanna, K.M., J.T. McNamara, and L. Lefrançois. 2007. In situ imaging of the endogenous CD8 T cell response to infection. *Science.* 318:116–120. doi:10.1126/science.1146291
- Krummel, M.F., M.D. Sjaastad, C. Wülfing, and M.M. Davis. 2000. Differential clustering of CD4 and CD3zeta during T cell recognition. *Science.* 289:1349–1352. doi:10.1126/science.289.5483.1349
- Labrecque, N., L.S. Whitfield, R. Obst, C. Waltzinger, C. Benoist, and D. Mathis. 2001. How much TCR does a T cell need? *Immunity.* 15:71–82. doi:10.1016/S1074-7613(01)00170-4
- Lankton, S., and A. Tannenbaum. 2008. Localizing region-based active contours. *IEEE Trans. Image Process.* 17:2029–2039. doi:10.1109/TIP.2008.2004611
- Lee, K.H., A.D. Holdorf, M.L. Dustin, A.C. Chan, P.M. Allen, and A.S. Shaw. 2002. T cell receptor signaling precedes immunological synapse formation. *Science.* 295:1539–1542. doi:10.1126/science.1067710
- Lee, K.H., A.R. Dinner, C. Tu, G. Campi, S. Raychaudhuri, R. Varma, T.N. Sims, W.R. Burack, H. Wu, J. Wang, et al. 2003. The immunological synapse balances T cell receptor signaling and degradation. *Science.* 302:1218–1222. doi:10.1126/science.1086507
- Liu, H., M. Rhodes, D.L. Wiest, and D.A. Vignali. 2000. On the dynamics of TCR:CD3 complex cell surface expression and downmodulation. *Immunity.* 13:665–675. doi:10.1016/S1074-7613(00)00066-2
- McGavern, D.B., U. Christen, and M.B. Oldstone. 2002. Molecular anatomy of antigen-specific CD8(+) T cell engagement and synapse formation in vivo. *Nat. Immunol.* 3:918–925. doi:10.1038/ni843
- Mempel, T.R., S.E. Henrickson, and U.H. Von Andrian. 2004. T-cell priming by dendritic cells in lymph nodes occurs in three distinct phases. *Nature.* 427:154–159. doi:10.1038/nature02238
- Miller, M.J., S.H. Wei, I. Parker, and M.D. Cahalan. 2002. Two-photon imaging of lymphocyte motility and antigen response in intact lymph node. *Science.* 296:1869–1873. doi:10.1126/science.1070051
- Miller, M.J., O. Safrina, I. Parker, and M.D. Cahalan. 2004. Imaging the single cell dynamics of CD4+ T cell activation by dendritic cells in lymph nodes. *J. Exp. Med.* 200:847–856. doi:10.1084/jem.20041236
- Monks, C.R., B.A. Freiberg, H. Kupfer, N. Sciaky, and A. Kupfer. 1998. Three-dimensional segregation of supramolecular activation clusters in T cells. *Nature.* 395:82–86. doi:10.1038/25764
- Negulescu, P.A., T.B. Krasieva, A. Khan, H.H. Kerschbaum, and M.D. Cahalan. 1996. Polarity of T cell shape, motility, and sensitivity to antigen. *Immunity.* 4:421–430. doi:10.1016/S1074-7613(00)80409-4
- Reichert, P., R.L. Reinhardt, E. Ingulli, and M.K. Jenkins. 2001. Cutting edge: in vivo identification of TCR redistribution and polarized IL-2 production by naive CD4 T cells. *J. Immunol.* 166:4278–4281.
- Revy, P., M. Sospedra, B. Barbour, and A. Trautmann. 2001. Functional antigen-independent synapses formed between T cells and dendritic cells. *Nat. Immunol.* 2:925–931. doi:10.1038/ni713
- Sawada, S., J.D. Scarborough, N. Killeen, and D.R. Littman. 1994. A lineage-specific transcriptional silencer regulates CD4 gene expression during T lymphocyte development. *Cell.* 77:917–929. doi:10.1016/0092-8674(94)90140-6
- Scholer, A., S. Hugues, A. Boissonnas, L. Fetler, and S. Amigorena. 2008. Intercellular adhesion molecule-1-dependent stable interactions between T cells and dendritic cells determine CD8+ T cell memory. *Immunity.* 28:258–270. doi:10.1016/j.immuni.2007.12.016
- Sims, T.N., T.J. Soos, H.S. Xenias, B. Dubin-Thaler, J.M. Hofman, J.C. Waite, T.O. Cameron, V.K. Thomas, R. Varma, C.H. Wiggins, et al. 2007. Opposing effects of PKC θ and WASp on symmetry breaking and relocation of the immunological synapse. *Cell.* 129:773–785. doi:10.1016/j.cell.2007.03.037

- Stefanová, I., J.R. Dorfman, and R.N. Germain. 2002. Self-recognition promotes the foreign antigen sensitivity of naive T lymphocytes. *Nature*. 420:429–434. doi:10.1038/nature01146
- Stoll, S., J. Delon, T.M. Brotz, and R.N. Germain. 2002. Dynamic imaging of T cell-dendritic cell interactions in lymph nodes. *Science*. 296:1873–1876. doi:10.1126/science.1071065
- Valitutti, S., S. Müller, M. Salio, and A. Lanzavecchia. 1997. Degradation of T cell receptor (TCR)-CD3- ζ complexes after antigenic stimulation. *J. Exp. Med.* 185:1859–1864. doi:10.1084/jem.185.10.1859
- Vardhana, S., K. Choudhuri, R. Varma, and M.L. Dustin. 2010. Essential role of ubiquitin and TSG101 protein in formation and function of the central supramolecular activation cluster. *Immunity*. 32:531–540. doi:10.1016/j.immuni.2010.04.005
- Varma, R., G. Campi, T. Yokosuka, T. Saito, and M.L. Dustin. 2006. T cell receptor-proximal signals are sustained in peripheral microclusters and terminated in the central supramolecular activation cluster. *Immunity*. 25:117–127. doi:10.1016/j.immuni.2006.04.010
- Worbs, T., T.R. Mempel, J. Bölder, U.H. von Andrian, and R. Förster. 2007. CCR7 ligands stimulate the intranodal motility of T lymphocytes in vivo. *J. Exp. Med.* 204:489–495. doi:10.1084/jem.20061706
- Wülfiging, C., J.D. Rabinowitz, C. Beeson, M.D. Sjaastad, H.M. McConnell, and M.M. Davis. 1997. Kinetics and extent of T cell activation as measured with the calcium signal. *J. Exp. Med.* 185:1815–1825. doi:10.1084/jem.185.10.1815
- Wülfiging, C., C. Sumen, M.D. Sjaastad, L.C. Wu, M.L. Dustin, and M.M. Davis. 2002. Costimulation and endogenous MHC ligands contribute to T cell recognition. *Nat. Immunol.* 3:42–47. doi:10.1038/ni741